Subgroup Discovery Points to the Prominent Role of Charge Transfer in Breaking Nitrogen Scaling Relations at Single-Atom Catalysts on VS$_2$

Haobo Li,* Yunxia Liu, Ke Chen, Johannes T. Margraf, Youyong Li, and Karsten Reuter

Read Online

ACCESS | 📊 Metrics & More | 📖 Article Recommendations | 🆘 Supporting Information

ABSTRACT: The electrochemical nitrogen reduction reaction (NRR) is a much sought-after low-energy alternative to Haber−Bosch ammonia synthesis. Single-atom catalysts (SACs) promise to break scaling relations between adsorption energies of key NRR reaction intermediates that severely limit the performance of extended catalysts. Here, we perform a computational screening study of transition metal (TM) SACs supported on vanadium disulfide (VS$_2$) and indeed obtain strongly broken scaling relations. A data-driven analysis by means of outlier detection and subgroup discovery reveals that this breaking is restricted to early TMs, while detailed electronic structure analysis rationalizes it in terms of strong charge transfer to the underlying support. This charge transfer selectively weakens *N and *NH adsorption and leads to promising NRR descriptors for SACs formed of earlier TMs like Ta that would conventionally not be associated with nitrogen reduction.

KEYWORDS: *subgroup discovery, density functional theory, computational screening, single-atom catalysts, electrochemical nitrogen reduction*
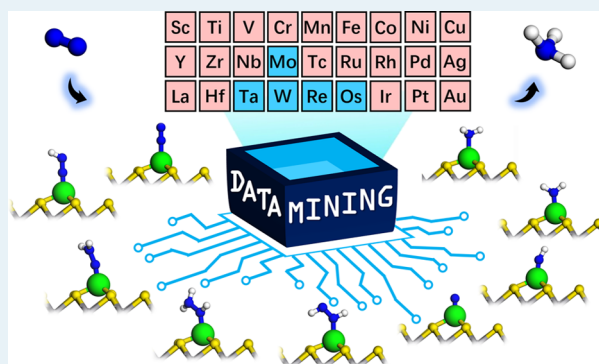
1. INTRODUCTION

Adding to its relevance for fertilizer or fiber production, NH$_3$ is increasingly pursued as an intermediate chemical for energy and hydrogen storage.[1−3] Developed in the early 20th century, the conventional Haber−Bosch process utilizes ruthenium- or iron-based catalysts for industrial ammonia synthesis under high temperature and high pressure, consuming large amounts of energy and releasing large amounts of greenhouse gases.[4] In particular, in conjunction with sustainably generated electricity, the electrochemical nitrogen reduction reaction (NRR) thus appears as a far superior approach to fix and hydrogenate N$_2$ to form NH$_3$ under ambient conditions.[5−9] At present, NRR is riddled with low faradic efficiencies and poor selectivity though.[10,11] For the most promising conventional transition metal (TM) catalysts Ru, Re, and Rh,[12] electrochemical benchmarking experiments in aqueous electrolyte yield no more ammonia than the background level of around 10 parts per billion, indicating that no ammonia is synthesized under the dominating hydrogen evolution reaction (HER).[13] This motivates strong research efforts to identify novel catalytic systems for the NRR.

Nitrogenase converts atmospheric nitrogen into ammonia under ambient conditions on the active site of TM sulfide (TMS) clusters.[14,15] Aiming to mimic this natural enzymatic process, catalysts based on extended TMSs indeed achieved high faradic efficiencies of over 20% recently.[16−18] Notwith-

standing, technological viability was estimated to require a faradic efficiency of ∼50% at a production rate of 10^{-4} mol h^{-1} cm^{-1}.[19,20] According to first-principles calculations, the potential-determining step (PDS) causing the high over-potentials for the NRR on most TMSs is the protonation of the adsorbed *NH intermediate to *NH$_2$.[21] Similar to the situation at extended TM surfaces,[11,22] engineering this step is limited by scaling relations that exist between the adsorption free energies of the *NH$_x$, *N$_2$, and *N$_2$H$_x$ intermediates involved in the reaction. Further improved NRR catalysts would thus either need to follow more suitable scaling relations or possibly even break them.

Constructing the specific active site structure is an effective strategy to break scaling relations and tune the reaction mechanism and selectivity.[23,24] With their unique isolated active site structure, single-atom catalysts (SACs) are an appealing catalyst class to this end[25−27]—apart from offering the maximum precious atom utilization.[28,29] First, SAC
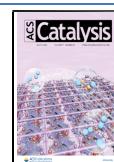
Scheme 1. Single-Atom Catalyst Systems and the NRR Reaction Mechanism[a]
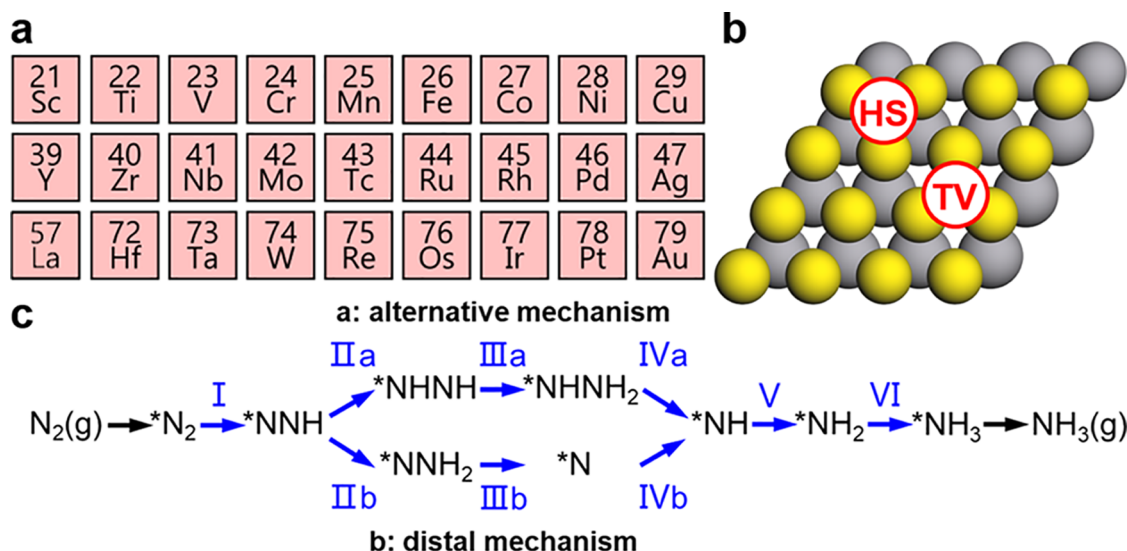
^{a}(a) Single-atom transition metals (TM$_1$s) considered in this work. (b) Top view of the hexagonal monolayer VS$_2$ substrate (V = large gray spheres and S = small yellow spheres), showing the employed (4 × 4) surface unit cell and the two 3-fold TM$_1$ adsorption sites: atop a VS$_2$ vanadium atom (TV) and atop a hollow formed by three S atoms (HS). (c) Associative NRR mechanism with six proton-coupled electron transfer (PCET) steps.

systems capable of the NRR at very low overpotentials of ∼−0.2 V (vs the reversible hydrogen electrode (RHE))[30−32] were indeed recently found. Other SACs were also reported to be able to suppress the HER and thus improve the NRR selectivity.[33] However, achieving high activity and selectivity simultaneously seems challenging for SACs with conventional two-dimensional (2D) substrates.[34,35]

In this situation, first reports have heralded the prospects of joining the two promising strands pursued for the NRR, i.e., to use extended TMSs as supports for single-atom transition metals (TM$_1$s).[36−39] Here, we aim to systematically explore this within a computational screening approach spanning a wide range of TM$_1$ all across the periodic system. We specifically select vanadium disulfide (VS$_2$) as a TM$_1$ supporting substrate, considering its earth-abundant composition, its excellent metallicity,[40] and its intrinsic poor activity toward the HER.[41−43] By generating a database of first-principles density functional theory (DFT) adsorption energies for NRR intermediates across 27 TM$_1$@VS$_2$ systems, we indeed find strongly broken scaling relations between calculated adsorption energies. Analyzing the data with outlier detection and subgroup discovery reveals that this break is restricted to early TM$_1$s though and is intriguingly not caused by the single-atom nature of the active TM$_1$. Instead, electronic structure analysis shows it to be a consequence of charge transfer to the VS$_2$ substrate, which selectively weakens the otherwise strong TM$_1$−N bonds for the earlier TM$_1$. While earlier TM$_1$s like Ta or W would fall onto the left leg of the NRR activity volcano if scaling relations were fully fulfilled, we now find them to exhibit highly promising low thermodynamic overpotentials.

2. METHODS

2.1. DFT Calculations. The DFT calculations were systematically performed in a spin-polarized way using the Quantum ESPRESSO (QE)[44] code and the van der Waals-corrected BEEF-vdW[45] functional to treat electronic exchange and correlation (see the Supporting Information (SI) for a

detailed account of the computational settings and the employed supercell containing a (4 × 4) surface unit cell). Ultrasoft pseudopotentials (USPP) were used for all calculations, and a Hubbard correction of $U = 3.0$ eV was applied to the d-orbitals of V.[46] As detailed in Table S1, test calculations were also conducted in a spin-polarized way with the HSE06[47] screened hybrid functional. These tests revealed the expected band gap opening[48] and partly quantitative changes of the computed adsorption energies, yet without challenging the identified break of scaling relations nor any of the conclusions taken from it.

2.2. Free Energies. Adsorption energies were calculated according to $E_{ad} = E_{adsorbate/surface} − E_{surface} − \mu_{adsorbate}$, where $E_{adsorbate/surface}$ and $E_{surface}$ are the total energies of the structurally relaxed TM$_1$@VS$_2$ system with and without adsorbate, respectively. $\mu_{adsorbate}$ refers to the chemical potential of N$_x$H$_y$ adsorbates as obtained from the gas-phase molecules N$_2$(g) and H$_2$(g) (Table S2). A more negative E_{ad} value corresponds to stronger binding between the adsorbate and the surface. Systematic tests described in the SI show the resulting E_{ad} to be numerically converged within 10 meV (Table S3). Adsorption free energies (G_{ad}) were then calculated as $G_{ad} = E_{ad} + \Delta G_{corr}$, where ΔG_{corr} contains the vibrational free energy correction (ZPE + $\int C_p dT − TS$, zero-point energy (ZPE), enthalpic temperature correction ($\int C_p dT$), and entropic correction (TS)) and the implicit solvation correction (ΔG_{sol}) calculated with the Environ module provided with QE,[49] as provided in Table S4. For the proton-coupled electron transfer (PCET) reaction steps, the effect of the applied potential is approximately accounted for within the thermodynamic computational hydrogen electrode (CHE) approach.[50] As the fingerprint of reactivity, the limiting potential U_L of a reaction step at the RHE scale results in the CHE simply as the potential at which the step becomes exergonic: $U_L = \Delta G_{ad}/e$, where ΔG_{ad} is the adsorption free energy difference between the two adsorbates after and before the PCET step, and e is the elementary negative charge. We denote the difference of the U_L of the PDS versus RHE as the
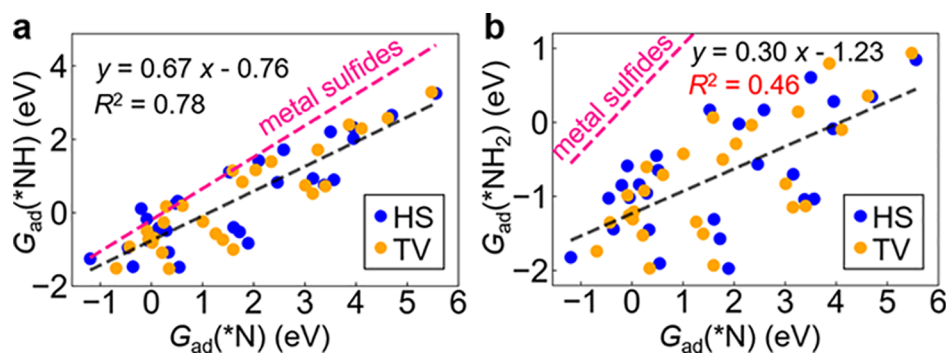
Figure 1. Distinctly broken adsorption energy scaling. Calculated adsorption free energies (G_{ad}) for *NH (a) and *NH$_2$ (b) versus the adsorption free energy of *N. Shown is data for all TM$_1$@VS$_2$ systems, with blue (orange) data points referring to TM$_1$ adsorption at the HS (TV) sites of the VS$_2$ support, cf. Scheme 1b. Gray dashed lines are linear fits to the data, with the slope, intercept, and R^2 coefficient explicitly stated. Pink dashed lines are corresponding fits from ref 21 to analog data for extended TMSs.

thermodynamic overpotential, $U_{L,PDS}$. This approximate computational quantity serves for the relative assessment of candidate systems and is not to be compared with experimental overpotentials, which are often also quoted with respect to the NRR equilibrium potential. Assuming a [NH$_4$OH] concentration of 10^{-7} M and 1 atm of N$_2$ in the aqueous solution, this equilibrium potential is, e.g., at 0.23 V versus RHE.[51,52]

2.3. Outlier Analysis and Subgroup Discovery. Subgroup discovery is a data mining approach to search, prune, and rank subgroups in given data sets that has recently also been applied in materials science[53,54] and SACs.[55] Here, we combine it with outlier detection, and specifically the random sample consensus (RANSAC) method. This method classifies data points into in- and outliers by repeatedly fitting linear models to random subsamples of the data and testing all data points against these hypothetical models (see the SI for details). This analysis is performed with the scikit-learn library. Subsequently, subgroup discovery (via the pysubgroup library) determines what the inliers have in common in terms of their key quantities. An example for such a subgroup would be all systems with a Pauling electronegativity (PE) between 1.0 and 2.0. All subgroups are then ranked according to a quality function, which reflects both the size of the subgroup and how well it differentiates between inliers and outliers. A detailed description of the subgroup definition and the quality function is provided in the SI.

3. RESULTS AND DISCUSSION

3.1. Adsorption Energies and Scaling Relations. Scheme 1 illustrates the 27 different TM$_1$ (TM = Sc−Cu; Y−Ag; La, Hf−Au) at the two high-symmetry sites of the hexagonal monolayer VS$_2$. For these SAC systems offering only one active adsorption site, a possible associative NRR mechanism[11] consisting of six proton-coupled electron transfer (PCET) steps is also shown in Scheme 1 and involves nine intermediates (*N$_2$, *NNH, *NNH$_2$, *NHNH, *NHNH$_2$, *N, *NH, *NH$_2$, and *NH$_3$). Adsorption free energies G_{ad} for all these intermediates at the different TM$_1$ and adsorption sites were systematically calculated with semilocal DFT, with a more negative G_{ad} indicating stronger binding. A first inspection of the generated data reveals that end-on adsorption for N$_2$ is almost always more stable than side-on adsorption (Figure S4), and so is *NNH$_2$ adsorption over *NHNH adsorption (Figure S5). The thermodynamic data thus suggest that the NRR at the considered SAC systems mostly follows an associative distal mechanism,[9] cf. Scheme 1c. Similar to the situation at extended TMS surfaces, binding of *N$_2$ and *NH$_3$ is largely independent of the TM$_1$ atom (Figure S6). While the evaluation of the limiting overpotential below explicitly considers the most stable adsorption configuration and the full preferred reaction path for each system, we correspondingly first focus our discussion on the adsorption of *NNH, *NNH$_2$, *N, *NH, and *NH$_2$ that critically governs the prevalent distal mechanism for most systems.

For these intermediates, linear scaling relations exist on extended TMs and TMSs that severely limit the NRR.[11,21,22] Effectively, all adsorption free energies of *N$_2$H$_x$ and *NH$_x$ scale linearly with G_{ad}(*N), and the phase space of possible thermodynamic overpotentials collapses to a one-dimensional volcano with minimum overpotentials found at Ru and RuS$_2$ for stepped TM and TMS surfaces, respectively.[11,21] Intriguingly, this is not the case for the present TM$_1$@VS$_2$ systems and we find a partially strong break of scaling relations. Figure 1 illustrates this for the *NH and *NH$_2$ intermediates. *NH binding is found to scale similarly well with *N binding as previously reported for extended TM and TMS surfaces. As compared to the latter, the TM$_1$@VS$_2$ systems bind *NH selectively somewhat stronger, as reflected in Figure 1a by a lower slope of the linear fitting line. They thus follow a more suitable scaling relation regarding the protonation of the adsorbed *NH intermediate to *NH$_2$ as further discussed below. In contrast, scaling is strongly broken for *NH$_2$, as visually apparent from Figure 1b and quantified by a low R^2 coefficient of 0.46 of the linear fit.

Further analysis of the adsorption free energies of all reaction intermediates (Figure S7) shows a simple systematics in the broken scaling relations. The calculated reaction intermediates separate into two groups. The adsorption of *NH, *NNH, and *NNH$_2$ scales well with the one of *N, consistently exhibiting high R^2 coefficients above 0.78. Adsorption of *NHNH and *NHNH$_2$ instead scales better with the one of *NH$_2$. Interestingly, it apparently makes a difference, whether the N atom directly coordinating to the TM$_1$ atom is additionally bound to at maximum one further atom (N or H) as in the first group or two atoms (two H atoms, or one N and one H atom) as in the second group.

Relevant for the preferred associative distal mechanism is thereby particularly the broken scaling relation between *N and *NH$_2$, as shown in Figure 1b. Unexpectedly, this break is not the result of the unique single-atom nature of the TM$_1$@VS$_2$ systems as compared to the previously studied extended

Scheme 2. Conceptual Data Analysis Workflow for a Hypothetical Data set[a]
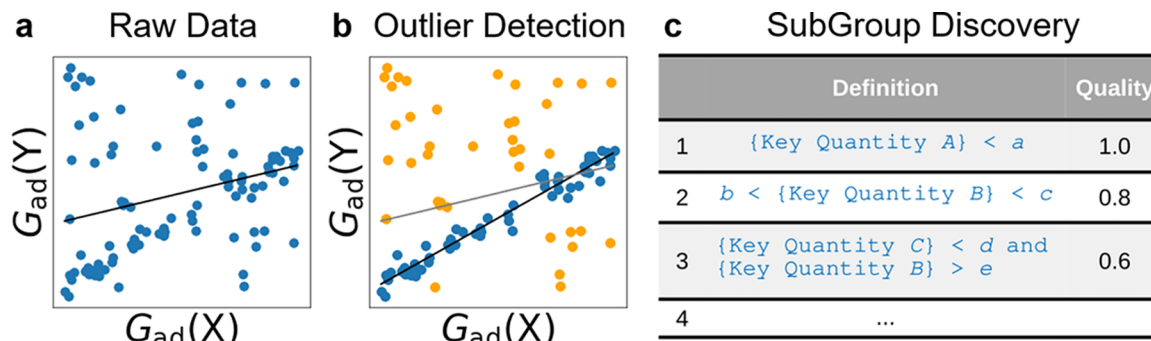
[a]While the raw data in the first frame indicates a weak correlation between two adsorption free energies ($G_{ad}(X)$ and $G_{ad}(Y)$), outlier detection indicates that this is due to the presence of outliers. Finally, subgroup discovery reveals that all inliers have in common that a key quantity A is smaller than some value a.
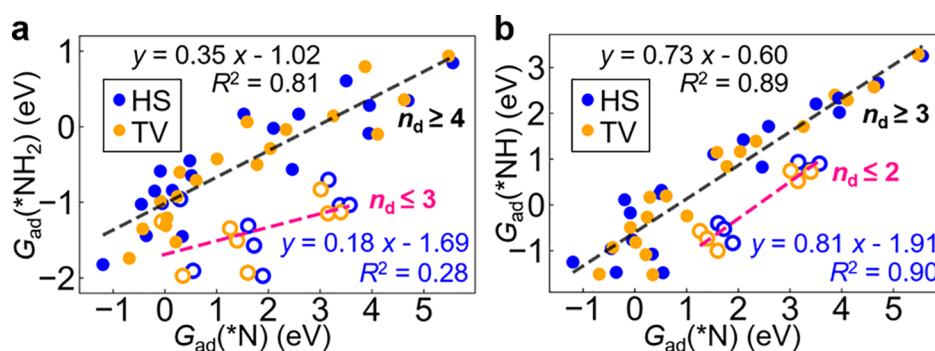

Figure 2. Adsorption energy scaling in subgroups. Same adsorption free energy data as shown in Figure 1, but now differentiating the identified subgroups. (a) For *NH$_2$, all TM$_1$@VS$_2$ systems with $n_d \geq 4$ (solid data points) fulfill the scaling relation with a high R^2 coefficient of 0.81, whereas the early TM$_1$@VS$_2$ systems with $n_d \leq 3$ (hollow data points) do not. (b) For *NH, this difference holds for TM$_1$@VS$_2$ systems with $n_d \geq 3$ (solid data points) and $n_d \leq 2$ (hollow data points), see text below.

TM[11] and TMS[21] surfaces. $G_{ad}(*N)$ and $G_{ad}(*NH_2)$ were calculated at the isolated TM$_1$ scale very well with each other, as expressed by a high R^2 coefficient of 0.84 (Figure S8). The break does not emerge as an indirect consequence of different adsorption geometries at the isolated TM$_1$ and at the TM$_1$ supported on the VS$_2$ substrate. If we recalculate the adsorption free energies at the isolated TM$_1$ for adsorption geometries fixed to the ones at the HS site on TM$_1$@VS$_2$ (i.e., we simply remove the substrate), the same good scaling is obtained as before ($R^2 = 0.82$). Intriguingly, the broken scaling between *N and *NH$_2$ adsorption is thus a purely electronic effect induced by the presence of the VS$_2$ support.

3.2. Scaling in TM$_1$ Subgroups. To further understand this electronic effect and its differentiated consequences for the various TM$_1$@VS$_2$ systems, we proceed by mining the computed database for further structure and correlations. For the targeted electronic effect, we thereby exploit the availability of additional information on the energetics and electronic structure as expressed in the following key quantities: Pauling electronegativity (PE), ionization potential (IP), electron affinity (EA), and number of electrons in the outermost d-shell (n_d) of the TM$_1$ atom; radius of d-orbitals (r_d), coupling matrix element squared (V_{ad}^2), and cohesive energy (E_{coh}) of the TM$_1$ bulk parent metal; energetic position of the d-band center (ϵ_d), Bader charge (q_{Bader}), and binding energy (E_b) of the TM$_1$ atom at the specific VS$_2$ adsorption site. All corresponding data for the 54 clean TM$_1$@VS$_2$ systems (27

TM$_1$ times 2 adsorption sites) are compiled in Tables S8 and S9 in the SI.

Suspecting that the scaling relations could be broken differently or to a differing degree over the 54 TM$_1$@VS$_2$ systems, we apply the random sample consensus (RANSAC) method to classify the data points into in- and outliers, followed by subgroup discovery to determine what the inliers have in common and what differentiates them from the outliers. Scheme 2 illustrates the applied workflow with full details provided in the SI. RANSAC indeed reveals good linear correlations for subsets of 30–40 TM$_1$@VS$_2$ inlier systems, depending on the residual threshold used to classify outliers (see the SI). The subsequent subgroup discovery analysis reveals that the single strongest predictor for whether a system belongs to the inliers is a membership to the subgroup $n_d > 4$. Conversely, the subgroup $n_d < 4$ representing the early TM$_1$s is an excellent predictor for the outliers. This leaves the systems with $n_d = 4$ as an edge case, which we treat as an inlier in the following. Notably, the outliers are also well predicted by the membership to the subgroup $q_{Bader} > 1.41$, in line with the interpretation that the breaking of scaling relations is related to charge transfer (see below).

If we thus replot the adsorption free energy data from Figure 1b and differentiate the two identified subgroups as done in Figure 2a, we indeed see that all TM$_1$@VS$_2$ systems with $n_d \geq 4$ obey a scaling relation between $G_{ad}(*N)$ and $G_{ad}(*NH_2)$, the same was found before for extended TM and TMS surfaces. It is only for the early TM$_1$ with $n_d \leq 3$ that the scaling is broken.
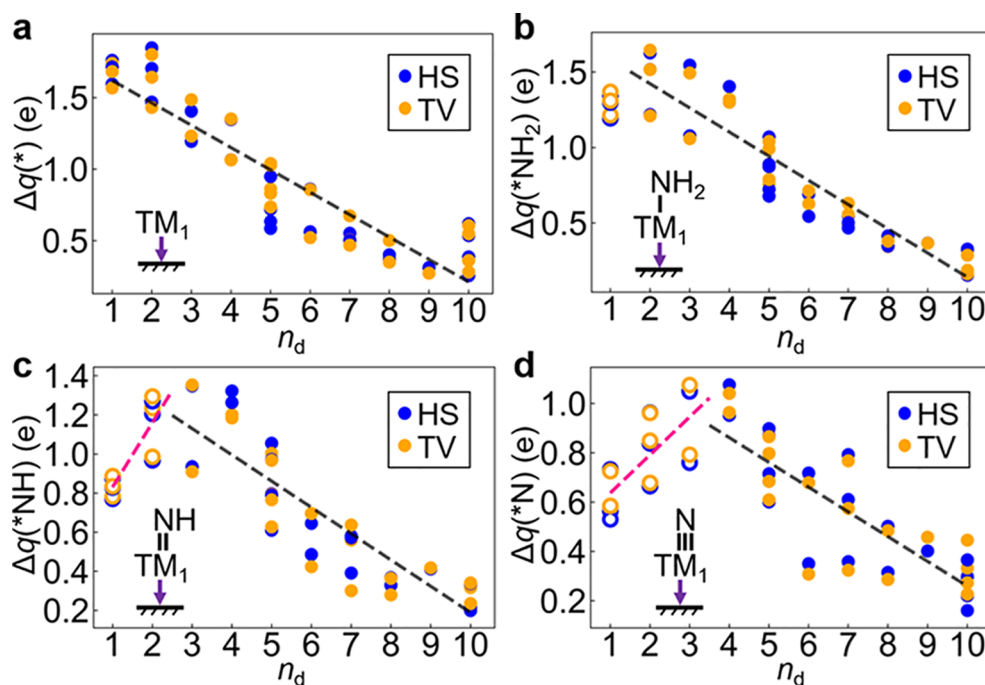
Figure 3. Charge competition between the adsorbate and the SAC support. Calculated charge transfer Δq from the TM_1 atom into the VS_2 support as a function of its number of outermost d-electrons (n_d). Shown are data for (a) the bare TM_1, as well as with (b) *NH_2, (c) *NH, and (d) *N adsorbed, and again considering the HS (blue data points) and TV (orange data points) TM_1 adsorption sites on the support. Δq is computed as the difference of Bader charge (q_{Bader}) on the TM_1 atom when isolated and when on the support, with a positive value indicating electron withdrawal from TM_1. The dashed lines are linear fits to the data to guide the eye.

This break results as a consequence of a change in the *N adsorption free energy with n_d. As shown in Figure S9, the binding strength does not continuously increase with decreasing n_d as is, e.g., the case for *NH_2 and the other reaction intermediates. Instead, it goes through a maximum for $n_d \sim 4$ to 5 and then decreases again.

This different trend can be rationalized in terms of charge competition between the adsorbate and the underlying support. As shown in Figure 3a, there is an increasing charge transfer Δq from the TM_1 atom to VS_2 with decreasing number of d-electrons, reflecting the decreasing TM_1 electronegativity when going toward the left of the periodic system. Upon adsorption of *NH_2, *NH, and *N (panels b−d in Figure 3) this amount of charge is progressively reduced. Moreover, comparatively less charge is transferred for early TM_1, breaking the linear trend over the TM series. In fact, the position where the linear trend in Δq reverses reflects the expected adsorption valency: For *NH_2 with a formal bond order of 1 to TM_1, Δq starts to only become less for $n_d = 1$ TM_1s. For *NH with an expected double bond, the trend changes for $n_d = 1-2$ TM_1s, while for *N with an expected formal triple bond, the trend changes for those with $n_d = 1-3$. For the electron scarce early TM_1s, the increasingly stronger adsorption thus reduces the amount of charge that can be transferred into the VS_2 support. At the same time, this still ongoing charge transfer to the support also limits the amount of charge available for the bonding to the electronegative adsorbates. As shown in Figure 3, we find comparatively less charge transferred to the nitrogen atom in the three adsorbates when the early TM_1s simultaneously have to satisfy the electron demand of the VS_2 support (Figure S10).

Conceptually spoken, under the simultaneous strong charge transfer to the support, the early TM_1 atoms do not have enough electrons to establish the full formal bond order to the *NH_x adsorbates and can correspondingly not bind them as strongly. It is clear that this limitation does not depend (much) on the specific TM_1 adsorption site and thus rationalizes why the break of scaling was independently found for both studied sites HS and TV. Selected Bader charge calculations with the screened hybrid HSE06 functional compiled in Table S10 further confirm that the employed semilocal DFT level adequately captures this charge competition picture despite its notorious charge delocalization problem. This competition for a limited amount of charge is quite different from the extended TM and TMS systems, where the electron availability is set by the Fermi level of the metallic surface. From this charge competition picture, it is also clear why the NRR intermediates seemed to separate into two groups, fulfilling or not fulfilling a scaling with G_{ad}(*N) depending on the number of N or H atoms bound to the TM_1-coordinating N atom (and thus determining the electron demand of the TM_1-N bond). In fact, with the differentiated understanding of Figure 3, we realize that the $n_d = 1-2$ $TM_1@VS_2$ systems should actually not exhibit a scaling between *NH and *N either. Since these are only few systems, this went unnoticed in Figure 1a and only contributed to a comparatively lower R^2 coefficient of 0.77 for the fitted scaling line. Indeed, if these systems are exempted, a much better fit with an R^2 coefficient of 0.89 is obtained, as shown in Figure 2b.

3.3. Effect on Limiting Potential. Having understood that and why the break of scaling relations is restricted to the earlier TM_1s, we return to the NRR and assess how it impacts a potential activity of $TM_1@VS_2$ catalysts. For this, we compute the limiting potentials for all reaction steps and identify the potential-determining step as the one with the most negative U_L of all PCET steps in the associative mechanism shown in
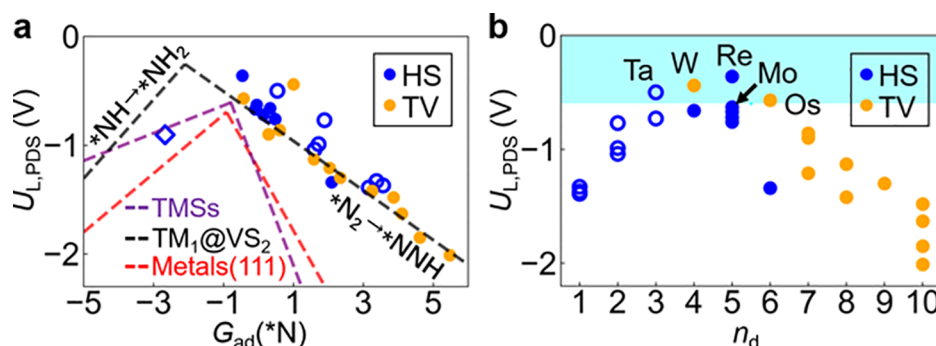
Figure 4. Thermodynamic overpotential for $TM_1@VS_2$ catalysts. $U_{L,PDS}$ versus RHE as a function of (a) $G_{ad}(*N)$ and (b) number of TM_1 d-electrons n_d. For each $TM_1@VS_2$ system, only the data for the more stable of the two adsorption sites (HS or TV) are shown (an analog figure containing the data for both sites is included in the SI as Figure S11). Data for early TM_1 ($n_d \leq 3$) affected by the break of scaling relation are drawn as hollow circles. The hollow diamond in (a) shows $U_{L,PDS}$ exhibited by $Ta_1@VS_2$ if it fulfilled the scaling relation (see text). For reference, the volcano-like activity curves resulting from the scaling-relation-dictated limiting potential of the $*NH \rightarrow *NH_2$ and $*N_2 \rightarrow *NNH$ steps are shown by dashed lines for the present $TM_1@VS_2$ fulfilling the scaling (black, cf. Figure S12), for extended TMs (red, from ref 11) and for extended TMSs via the associative mechanism (purple, from ref 21).
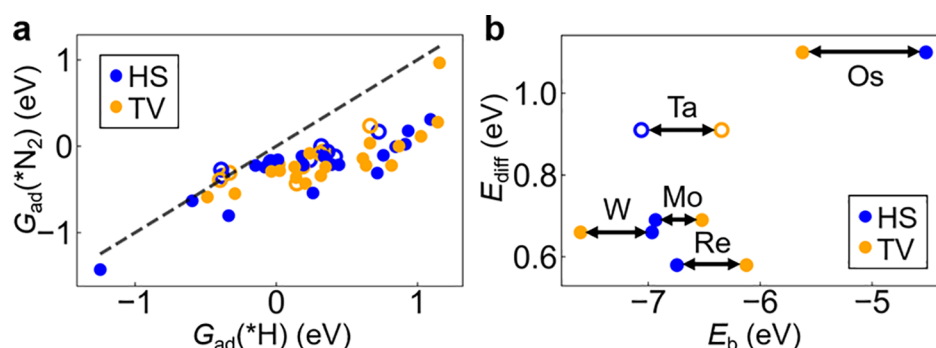

Figure 5. SAC selectivity and stability. (a) Comparison of $G_{ad}(*N_2)$ versus $G_{ad}(*H)$ indicating a generally high selectivity toward the NRR for the $TM_1@VS_2$ systems (for both TM_1 adsorption sites). (b) Diffusion barrier (E_{diff}) between HS and TV sites of TM_1 on the VS_2 support versus the TM_1 binding energy (E_b) to the support for the five TM_1s exhibiting least negative overpotentials, cf. Figure 4b.

Scheme 1, with the reaction path always following the branches with less negative U_L. We denote the difference of this U_L of the PDS versus RHE as the thermodynamic overpotential, $U_{L,PDS}$, which an ideal NRR catalyst would minimize, and compile all corresponding $U_{L,PDS}$ data in Table S11. The actual PDS is $*N_2 \rightarrow *NNH$ for all $TM_1@VS_2$ except for W_1, for which the $U_{L,PDS}(*NNH_2 \rightarrow *N)$ of -0.39 V for the HS site and $U_{L,PDS}(*NH_2 \rightarrow *NH_3)$ of -0.44 V for the TV site are both very close to the $U_L = -0.33$ and -0.29 V of the $*N_2 \rightarrow *NNH$ step, respectively. Figure 4a shows the resulting thermodynamic overpotential $U_{L,PDS}$ set by the potential-determining step for all $TM_1@VS_2$ systems as a function of $G_{ad}(*N)$. Also included in the figure is the typical volcano-like activity line that is imposed by the limiting potentials of the $*NH \rightarrow *NH_2$ (left leg of the volcano) and $*N_2 \rightarrow *NNH$ (right leg of the volcano) reaction steps if these fully fulfilled the linear scaling relations. For the $TM_1@VS_2$ systems, we here specifically used the fits included in Figure 2 to the subgroup that actually does fulfill scaling, see also Figure S12. While early TMs fall on the corresponding left leg of the volcano for extended TMs[11] and TMSs[21] catalysts, this is not the case for the present SAC systems. What the above-discussed charge-transfer-induced selective weakening of the $*N$ binding behind the break of scaling does for these early TM_1s is thus to shift them to the right of the volcano, as shown in Figure 4a. We illustrate this specifically for Ta_1 at its more stable HS site at VS_2 in Figure 4a, where we include the corresponding data

point (hollow diamond) if Ta_1 fulfilled the scaling relations. It would then exhibit much stronger $G_{ad}(*N)$, would be limited by the $*NH \rightarrow *NH_2$ step, and would exhibit a more than 0.5 V higher thermodynamic overpotential.

Ultimately, the charge-transfer-induced break of scaling thus allows some of the early $TM_1@VS_2$ to attain lower thermodynamic overpotentials. However, also the larger group of $TM_1@VS_2$ that does fulfill scaling exhibits superior NRR capabilities than traditional extended TM and TMS catalysts. This is apparent from Figure 4a, where the volcano curves for the latter systems as established in the literature[11,21] are also included. Most notably, the right leg of the SAC volcano exhibits a much smaller negative slope than the ones of the extended systems, allowing more $TM_1@VS_2$ systems to exhibit appealing least negative $U_{L,PDS}$. In other words, the volcano is wider and a wider range of $G_{ad}(*N)$ leads to acceptably low overpotentials. The reason behind this is the more favorable scaling shown in Figure 1a, with a somewhat stronger selective $*NH$ binding, e.g., on the extended TMS. In other words, still somewhat weaker selective $*N$ binding is eventually also a consequence of the charge transfer to the VS_2 support. As recently also highlighted by Hulva et al.[56] charge transfer is thus in many respects a crucial aspect for the performance and optimization of SACs. What it implies in terms of the optimum TM_1 species is clearly seen when replotting the thermodynamic overpotential data as a function of the number of TM_1 d-electrons n_d, as shown in Figure 4b.

As expected, this also yields a volcano. However, intriguingly, the top of the volcano is now located around $n_d \sim 4$ to 5 and the five most active TM_1s are Ta_1, W_1, Re_1, Mo_1, and Os_1, all showing $U_{L,PDS} > -0.6$ V, cf. Table S11. In contrast, for extended systems, the highest activity is rather found for TMs further to the right in the periodic system, with most active extended TMs being Re, Ru, or Rh with $n_d = 5-8$, and most active TMSs being RuS_2 or FeS_2 with $n_d = 6-7$. Effectively, the support thus somewhat skews the volcano to the left bringing an element like W into the game that is to the least substantially more abundant than traditional Ru.

3.4. Selectivity and Stability. Of course, the thermodynamic overpotential is a descriptor that only probes NRR activity. Selectivity against the competing HER and the overall stability of the SAC against sintering are equally important aspects. Also to this end, the present $TM_1@VS_2$ systems appear highly promising. Figure 5a compares the adsorption strength of $*N_2$ to the one of $*H$, which for the prevalent associative distal NRR mechanism can be used as a selectivity descriptor. All studied $TM_1@VS_2$ systems exhibit similar strength or even a clear preference for $*N_2$ adsorption. This holds in particular for the five most active TM_1 in Figure 4b, for which we provide the explicit $G_{ad}(*N_2) - G_{ad}(*H)$ values in Table S12. These top five TM_1 further exhibit strong binding to the VS_2 support in excess of -4.5 eV, as shown in Figure 5b. For comparison, for Co_1 supported on MoS_2 with an experimentally validated stability, a comparatively weaker binding of only -4 eV has been reported.[57] While this suggests good overall stability at the support, a high diffusion barrier over the support is particularly indicative of stability against sintering. Diffusion barriers of the order of ~ 1 eV have, e.g., been calculated for the experimentally synthesized Pd_1 supported on C_3N_4 SAC systems.[58] Compared to this, we find somewhat smaller barriers for W_1, Re_1, and Mo_1, while in particular, Ta_1 and Os_1 exhibit barriers of the same size as those of the experimentally realized system. Note that, intriguingly and as discussed above, Ta_1 belongs to the $n_d \leq 3$ subgroup and exhibits high NRR performance only because of the break of scaling relations.

4. CONCLUSIONS

Apart from their unique precious material efficiency, SAC systems are generally hoped to exhibit more favorable scaling relations (or even break them) than those known to limit the NRR performance of extended TM or TMS catalysts. Our systematic screening of $TM_1@VS_2$ SAC systems indeed reveals such strongly broken scaling of adsorption energies of the key reaction intermediates $*N$ and $*NH_2$. Modern data analysis in the form of outlier detection and subgroup discovery allows us to differentiate this intriguing finding. In fact, the scaling relations are only broken for early TM_1s and detailed electronic structure analysis rationalizes this in terms of competition for the charge between the adsorbate(s) and the underlying support. The strong charge transfer to the VS_2 support selectively weakens in particular the adsorption of stronger binding intermediates like $*N$ and $*NH$. This leads to more favorable thermodynamic NRR overpotentials of some early TM_1s (that break scaling) and late TM_1s (that obey scaling) alike.

The top $TM_1@VS_2$ systems exhibit thermodynamic overpotentials that are significantly smaller than those previously calculated for extended TM and TMS catalysts. They furthermore exhibit descriptors that suggest good selectivity

against the competing HER and good stability against sintering. While computed thermodynamic overpotentials cannot straightforwardly be compared to measured overpotentials, the values of around -0.4 V versus RHE obtained here for the top $TM_1@VS_2$ seem not incompatible with best performing other SAC systems highlighted recently in the literature.[59−61] With selectivity arguably more important than activity, another central insight of our study is the role of charge transfer to the support, to which we were led by data mining. For the present systems, this charge transfer skews the activity volcano toward earlier transition metals and, for example, brings W_1 or Ta_1 rather than extended Ru or RuS_2 up on the agenda.

We expect these detailed insights into the role of charge transfer to generalize to other SAC support materials (both other TM_1-doped metal sulfide supports and other support classes like metal carbides or metal nitrides). In fact, tuning the amount of charge transfer could be a decisive means to a controlled break of scaling relations in SAC catalysis. From our present results, we hypothesize that a support that induces an even stronger charge transfer than VS_2 would be desirable for the NRR to further skew the activity volcano toward earlier transition metals. A concomitant detailed assessment of different support materials to validate this hypothesis and, in general, engineering of charge transfer are correspondingly clear objectives for future SAC development.

■ ASSOCIATED CONTENT

ⓢ Supporting Information

The Supporting Information is available free of charge at https://pubs.acs.org/doi/10.1021/acscatal.1c01324.

> Additional DFT and subgroup discovery details; additional comparisons of adsorption free energies; additional scaling relation plots; additional charge differences; and $U_{L,PDS}$ across $TM_1@VS_2$ (PDF)

■ AUTHOR INFORMATION

Corresponding Author

Haobo Li − *Chair for Theoretical Chemistry and Catalysis Research Center, Technische Universität München, 85747 Garching, Germany;* ⓞ orcid.org/0000-0002-9448-6771; Email: haobo.li@ch.tum.de

Authors

Yunxia Liu − *Chair for Theoretical Chemistry and Catalysis Research Center, Technische Universität München, 85747 Garching, Germany; Institute of Functional Nano & Soft Materials (FUNSOM), Jiangsu Key Laboratory for Carbon-Based Functional Materials and Devices, Joint International Research Laboratory of Carbon-Based Functional Materials and Devices, Soochow University, Suzhou 215123, P. R. China*

Ke Chen − *Chair for Theoretical Chemistry and Catalysis Research Center, Technische Universität München, 85747 Garching, Germany; Fritz-Haber-Institut der Max-Planck-Gesellschaft, 14195 Berlin, Germany*

Johannes T. Margraf − *Chair for Theoretical Chemistry and Catalysis Research Center, Technische Universität München, 85747 Garching, Germany; Fritz-Haber-Institut der Max-Planck-Gesellschaft, 14195 Berlin, Germany*

Youyong Li − *Institute of Functional Nano & Soft Materials (FUNSOM), Jiangsu Key Laboratory for Carbon-Based*

Functional Materials and Devices, Joint International Research Laboratory of Carbon-Based Functional Materials and Devices, Soochow University, Suzhou 215123, P. R. China; orcid.org/0000-0002-5248-2756

Karsten Reuter − *Chair for Theoretical Chemistry and Catalysis Research Center, Technische Universität München, 85747 Garching, Germany; Fritz-Haber-Institut der Max-Planck-Gesellschaft, 14195 Berlin, Germany;* orcid.org/0000-0001-8473-8659

Complete contact information is available at:
https://pubs.acs.org/10.1021/acscatal.1c01324

REFERENCES

(1) Erisman, J. W.; Sutton, M. A.; Galloway, J.; Klimont, Z.; Winiwarter, W. How a century of ammonia synthesis changed the world. *Nat. Geosci.* **2008**, *1*, 636−639.

(2) Appl, M. Ammonia, 1. Introduction. In *Ullmann's encyclopedia of industrial chemistry*; Wiley-VCH: Weinheim, Germany, 2011.

(3) van der Ham, C. J. M.; Koper, M. T. M.; Hetterscheid, D. G. Challenges in reduction of dinitrogen by proton and electron transfer. *Chem. Soc. Rev.* **2014**, *43*, 5183−5191.

(4) Jennings, J. R. *Catalytic Ammonia Synthesis: Fundamentals and Practice*; Plenum: New York, 1991.

(5) Norskov, J.; Chen, J.; Miranda, R.; Fitsimmon, T.; Stack, R. *Sustainable Ammonia Synthesis - Exploring the Scientific Challenges Associated with Discovering Alternative, Sustainable Processes for Ammonia Production*; United States Department of Energy, 2016.

(6) Kim, K.; Lee, N.; Yoo, C.-Y.; Kim, J.-N.; Yoon, H. C.; Han, J.-I. Communication - electrochemical reduction of nitrogen to ammonia in 2-propanol under ambient temperature and pressure. *J. Electrochem. Soc.* **2016**, *163*, F610−F612.

(7) Liu, H.; Wei, L.; Pei, Z.; Shi, J.; Wang, Z.; He, D.; Chen, Y.; Liu, F. Homogeneous, heterogeneous, and biological catalysts for electrochemical N2 reduction toward NH3 under ambient conditions. *ACS Catal.* **2019**, *9*, 5245−5267.

(8) Tang, C.; Qiao, S.-Z. How to explore ambient electrocatalytic nitrogen reduction reliably and insightfully. *Chem. Soc. Rev.* **2019**, *48*, 3166−3180.

(9) Manjunatha, R.; Karajic, A.; Liu, M.; Zhai, Z.; Dong, L.; Yan, W.; Wilkinson, D. P.; Zhang, J. A Review of Composite/Hybrid Electrocatalysts and Photocatalysts for Nitrogen Reduction Reactions: Advanced Materials, Mechanisms, Challenges and Perspectives. *Electrochem. Energ. Rev.* **2020**, *3*, 506−540.

(10) Singh, A. R.; Rohr, B. A.; Schwalbe, J. A.; Cargnello, M.; Chan, K.; Jaramillo, T. F.; Chorkendorff, I.; Norskov, J. K. Electrochemical ammonia synthesis - the selectivity challenge. *ACS Catal.* **2017**, *7*, 706−709.

(11) Skúlason, E.; Bligaard, T.; Gudmundsdottir, S.; Studt, F.; Rossmeisl, J.; Abild-Pedersen, F.; Vegge, T.; Jonsson, H.; Norskov, J. K. A theoretical evaluation of possible transition metal electro-catalyst for N2 reduction. *Phys. Chem. Chem. Phys.* **2012**, *14*, 1235−1245.

(12) Montoya, J. H.; Tsai, C.; Vojvodic, A.; Norskov, J. K. The challenge of electrochemical ammonia synthesis: a new perspective on the role of nitrogen scaling relations. *ChemSusChem* **2015**, *8*, 2180−2186.

(13) Andersen, S. Z.; Colic, V.; Yang, S.; Schwalbe, J. A.; Nielander, A. C.; McEnaney, J. M.; Enemark-Rasmussen, K.; Baker, J. G.; Singh, A. R.; Rohr, B. A.; Statt, M. J.; Blair, S. J.; Mezzavilla, S.; Kibsgaard, J.; Vesborg, P. C. K.; Cargnello, M.; Bent, S. F.; Jaramillo, T. F.; Stephens, I. E. L.; Norskov, J. K.; Chorkendorff, I. A rigorous electrochemical ammonia synthesis protocol with quantitative isotope measurements. *Nature* **2019**, *570*, 504−508.

(14) Burgess, B. K.; Lowe, D. J. Mechanism of molybdenum nitrogenase. *Chem. Rev.* **1996**, *96*, 2983−3011.

(15) Bukas, V. J.; Norskov, J. K. A molecular-level mechanism of the biological N2 fixation. *ChemRxiv* Preprint DOI: 10.26434/chemrxiv.10029224.v1.

(16) Chen, P.; Zhang, N.; Wang, S.; Zhou, T.; Tong, Y.; Ao, C.; Yan, W.; Zhang, L.; Chu, W.; Wu, C.; Xie, Y. Interfacial engineering of cobalt sulfide/graphene hybrids for highly efficient ammonia electrosynthesis. *Proc. Natl. Acad. Sci. U.S.A.* **2019**, *116*, 6635−6640.

(17) Nan, H.; Liu, Y.; Li, Q.; Shen, P.; Chu, K. A Janus antimony sulfide catalyst for highly selective N2 electroreduction. *Chem. Commun.* **2020**, *56*, 10345−10348.

(18) Xu, X.; Tian, X.; Sun, B.; Liang, Z.; Cui, H.; Tian, J.; Shao, M. 1 T-phase molybdenum sulfide nanodots enable efficient electrocatalytic nitrogen fixation under ambient conditions. *Appl. Catal., B* **2020**, *272*, No. 118984.

(19) Xu, H.; Ithisuphalap, K.; Li, Y.; Mukherjee, S.; Lattimer, J.; Soloveichik, G.; Wu, G. Electrochemical ammonia synthesis through N2 and H2O under ambient conditions: theory, practices, and challenges for catalysts and electrolytes. *Nano Energy* **2020**, *69*, No. 104469.

(20) Foster, S. L.; Bakovic, S. I. P.; Duda, R. D.; Maheshwari, S.; Milton, R. D.; Minteer, S. D.; Janik, M. J.; Renner, J. N.; Greenlee, L. F. *Nat. Catal.* **2018**, *1*, 490−500.

(21) Abghoui, Y.; Sigtryggsson, S. B.; Skulason, E. Biomimetic nitrogen fixation catalyzed by transition metal sulfide surfaces in an electrolytic cell. *ChemSusChem* **2019**, *12*, 4265−4273.

(22) Abild-Pedersen, F.; Greeley, J.; Studt, F.; Rossmeisl, J.; Munter, T. R.; Moses, P. G.; Skulason, E.; Bligaard, T.; Norskov, J. K. Scaling properties of adsorption energies for hydrogen-containing molecules on transition-metal surfaces. *Phys. Rev. Lett.* **2007**, *99*, No. 016105.

(23) Reuter, K.; Plaisance, C. P.; Oberhofer, H.; Andersen, M. Perspective: On the active site model in computational catalyst screening. *J. Chem. Phys.* **2017**, *146*, No. 040901.

(24) Li, H.; Reuter, K. Active-site computational screening: Role of structural and compositional diversity for the electrochemical CO2 reduction at Mo carbide catalysts. *ACS Catal.* **2020**, *10*, 11814−11821.

(25) Sun, G.; Zhao, Z.-J.; Mu, R.; Zha, S.; Li, L.; Chen, S.; Zang, K.; Luo, J.; Li, Z.; Purdy, S. C.; Kropf, A. J.; Miller, J. T.; Zeng, L.; Gong, J. Breaking the scaling relationship via thermally stable Pt/Cu single

atom alloys for catalytic dehydrogenation. *Nat. Commun.* **2018**, *9*, No. 4454.

(26) Zhao, Z.-J.; Liu, S.; Zha, S.; Cheng, D.; Studt, F.; Henkelman, G.; Gong, J. Theory-guided design of catalytic materials using scaling relationships and reactivity descriptors. *Nat. Rev. Mater.* **2019**, *4*, 792−804.

(27) Darby, M. T.; Stamatakis, M.; Michaelides, A.; Sykes, E. C. H. Lonely atoms with special gifts: Breaking linear scaling relations in heterogeneous catalysis with single-atom alloys. *J. Phys. Chem. Lett.* **2018**, *9*, 5636−5646.

(28) Zhu, C.; Fu, S.; Shi, Q.; Du, D.; Lin, Y. Single-atom electrocatalysts. *Angew. Chem., Int. Ed.* **2017**, *56*, 13944−13960.

(29) Lu, B.; Liu, Q.; Chen, S. Electrocatalysis of single-atom sites: impacts of atomic coordination. *ACS Catal.* **2020**, *10*, 7584−7618.

(30) Tao, H.; Choi, C.; Ding, L.-X.; Jiang, Z.; Han, Z.; Jia, M.; Fan, Q.; Gao, Y.; Wang, H.; Robertson, A. W.; Hong, S.; Jung, Y.; Liu, S.; Sun, Z. Nitrogen fixation by Ru single-atom electrocatalytic reduction. *Chem* **2019**, *5*, 204−214.

(31) Geng, Z.; Liu, Y.; Kong, X.; Li, P.; Li, K.; Liu, Z.; Du, J.; Shu, M.; Si, R.; Zeng, J. Electrochemical reduction over Ru single-atom catalysts. *Adv. Mater.* **2018**, *30*, No. 1803498.

(32) Zhao, J.; Chen, Z. Single Mo atom supported on defective boron nitride monolayer as an efficient electrocatalyst for nitrogen fixation: a computational study. *J. Am. Chem. Soc.* **2017**, *139*, 12480−12487.

(33) Choi, C.; Back, S.; Kim, N.-Y.; Lim, J.; Kim, Y.-H.; Jung, Y. Suppression of hydrogen evolution reaction in electrochemical N2 reduction using single-atom catalysts: a computational guideline. *ACS Catal.* **2018**, *8*, 7517−7525.

(34) Li, L.; Martirez, M. P.; Carter, E. Prediction of highly selective electrocatalyic nitrogen reduction low overpotential on a Mo-doped g-GaN monolayer. *ACS Catal.* **2020**, *10*, 12841−12857.

(35) Tang, S.; Dang, Q.; Liu, T.; Zhang, S.; Zhou, Z.; Li, X.; Wang, X.; Sharman, E.; Luo, Y.; Jiang, J. Realizing a not-strong-not-weak polarization electric field in single-atom catalysts sandwiched by boron nitride and graphene sheets for efficient nitrogen fixation. *J. Am. Chem. Soc.* **2020**, *142*, 19308−19315.

(36) Zhu, J.; Cai, L.; Yin, X.; Wang, Z.; Zhang, L.; Ma, H.; Ke, Y.; Du, Y.; Xi, S.; Wee, A. T. S.; Chai, Y.; Zhang, W. Enhanced electrocatalytic hydrogen evolution activity in single-atom Pt-decorated VS2 nanosheets. *ACS Nano* **2020**, *14*, 5600−5608.

(37) Ma, X.; Hu, J.; Zheng, M.; Li, D.; Lv, H.; He, H.; Huang, C. N2 reduction using single transition-metal atom supported on defective WS2 monolayer as promising catalysts: a DFT study. *Appl. Surf. Sci.* **2019**, *489*, 684−692.

(38) Guo, H.; Li, L.; Wang, X.; Yao, G.; Yu, H.; Tian, Z.; Li, B.; Chen, L. Theoretical investigation on the single transition-metal atom-decorated defective MoS2 for electrocatalytic ammonia synthesis. *ACS Appl. Mater. Interfaces* **2019**, *11*, 36506−36514.

(39) Deng, J.; Li, H.; Xiao, J.; Tu, Y.; Deng, D.; Yang, H.; Tian, H.; Li, J.; Ren, P.; Bao, X. Triggering the electrocatalytic hydrogen evolution activity of the inert two-dimensional MoS2 surface via single-atom metal doping. *Energy Environ. Sci.* **2015**, *8*, 1594−1601.

(40) Feng, J.; Sun, X.; Wu, C.; Peng, L.; Lin, C.; Hu, S.; Yang, J.; Xie, Y. Metallic few-layered VS2 ultrathin nanosheets: High tow-dimensional conductivity for in-plane supercapacitors. *J. Am. Chem. Soc.* **2011**, *133*, 17832−17838.

(41) Zhang, J.; Zhang, C.; Wang, Z.; Zhu, J.; Wen, Z.; Zhao, X.; Zhang, X.; Xu, J.; Lu, Z. Synergistic interlayer and defect engineering in VS2 nanosheets toward efficient electrocatalytic hydrogen evolution reaction. *Small* **2018**, *14*, No. 1703098.

(42) Chia, X.; Ambrosi, A.; Lazar, P.; Sofer, Z.; Pumera, M. Electrocatalysis of layered group 5 metallic transition metal dichalcogenides (MX2, M = V, Nb, and Ta; X = S, Se, and Te). *J. Mater. Chem. A* **2016**, *4*, 14241−14253.

(43) Chen, X.; Yu, K.; Shen, Y.; Feng, Y.; Zhu, Z. Synergistic effect of MoS2 nanosheets and VS2 for the hydrogen evolution reaction with enhanced humidity-sensing performance. *ACS Appl. Mater. Interfaces* **2017**, *9*, 42139−42148.

(44) Gianozzi, P.; et al. QUANTUM ESPRESSO: A modular and open-source software project for quantum simulations of materials. *J. Phys.: Condens. Matter* **2009**, *21*, No. 395502.

(45) Wellendorff, J.; Lundgaard, K. T.; Mogelhoj, A.; Petzold, V.; Landis, D. D.; Norskov, J. K.; Bligaard, T.; Jacobsen, K. W. Density functionals for surface science: Exchange-correlation model development with Bayesian error estimation. *Phys. Rev. B* **2012**, *85*, No. 235149.

(46) Isaacs, E. B.; Marianetti, C. A. Electronic correlations in monolayer VS2. *Phys. Rev. B* **2016**, *94*, No. 035120.

(47) Krukau, A. V.; Vydrov, O. A.; Izmaylov, A. F.; Scuseria, G. E. Influence of the exchange screening parameter on the performance of screened hybrid functionals. *J. Chem. Phys.* **2006**, *125*, No. 224106.

(48) Jing, Y.; Zhou, Z.; Cabrera, C. R.; Chen, Z. Metallic VS2 monolayer: a promising 2D anode material for lithium ion batteries. *J. Phys. Chem. C* **2013**, *117*, 25409−25413.

(49) Andreussi, O.; Hoermann, N. G.; Nattino, F.; Fisicaro, G.; Goedeck-er, S.; Marzari, N. Solvent-aware interfaces in continuum solva-tion. *J. Chem. Theory. Comput.* **2019**, *15*, 1996−2009.

(50) Nørskov, J. K.; Rossmeisl, J.; Logadottir, A.; Lindqvist, L.; Kitchin, J. R.; Bligaard, T.; Jonsson, H. Origin of the overpotential for oxygen reduction at a fuel-cell cathode. *J. Phys. Chem. B* **2004**, *108*, 17886−17892.

(51) Lindley, B. M.; Appel, A. M.; Krogh-Jespersen, K.; Mayer, J. M.; Miller, A. J. M. Evaluating the thermodynamics of electrocatalytic N2 reduction in Acetonitrile. *ACS Energy Lett.* **2016**, *1*, 698−704.

(52) Tang, C.; Qiao, S.-Z. How to explore ambient electrocatalytic nitrogen reduction reliably and insightfully. *Chem. Soc. Rev.* **2019**, *48*, 3166−3180.

(53) Goldsmith, B. R.; Boley, M.; Vreeken, J.; Scheffler, M.; Ghiringhelli, L. M. Uncovering structure-property relationships of materials by subgroup discovery. *New J. Phys.* **2017**, *19*, No. 013031.

(54) Sutton, C.; Boley, M.; Ghiringhelli, L. M.; Rupp, M.; Vreeken, J.; Scheffler, M. Identifying domains of applicability of machine learning models for materials science. *Nat. Commun.* **2020**, *11*, No. 4428.

(55) Han, Z. K.; Sarker, D.; Ouyang, R.; Mazheika, A.; Gao, Y.; Levchenko, S. V. Single-atom alloy catalysts designed by first-principles calculations and artificial intelligence. *Nat. Commun.* **2021**, *12*, No. 1833.

(56) Hulva, J.; Meier, M.; Bliem, R.; Jakub, Z.; Kraushofer, F.; Schmid, M.; Diebold, U.; Franchini, C.; Parkinson, G. S. Unraveling CO adsorption on model single-atom catalysts. *Science* **2021**, *371*, 375−379.

(57) Qi, K.; Cui, X.; Gu, L.; et al. Single-atom cobalt array bound to distorted 1T MoS2 with ensemble effect for hydrogen evolution catalysis. *Nat. Commun.* **2019**, *10*, No. 5231.

(58) Vilé, G.; Albani, D.; Nachtegaal, M.; Chen, Z.; Dontsova, D.; Antonietti, M.; Lopez, N.; Perez-Ramirez, J. A stable single-site palladium catalyst for hydrogenations. *Angew. Chem., Int. Ed.* **2015**, *54*, 11265−11269.

(59) Tao, H.; Choi, C.; Ding, L.-X.; Jiang, Z.; Han, Z.; Jia, M.; Fan, Q.; Gao, Y.; Wang, H.; Robertson, A. W.; Hong, S.; Jung, Y.; Liu, S.; Sun, Z. Nitrogen fixation by Ru single-atom electrocatalytic reduction. *Chem* **2019**, *5*, 204−214.

(60) Geng, Z.; Liu, Y.; Kong, X.; Li, P.; Li, K.; Liu, Z.; Du, J.; Shu, M.; Si, R.; Zeng, J. Electrochemical reduction over Ru single-atom catalysts. *Adv. Mater.* **2018**, *30*, No. 1803498.

(61) Zhao, J.; Chen, Z. Single Mo atom supported on defective boron nitride monolayer as an efficient electrocatalyst for nitrogen fixation: a computational study. *J. Am. Chem. Soc.* **2017**, *139*, 12480−12487.